Report

Cell Reports

Structural Basis for Receptor-Mediated Selective Autophagy of Aminopeptidase I Aggregates

Graphical Abstract

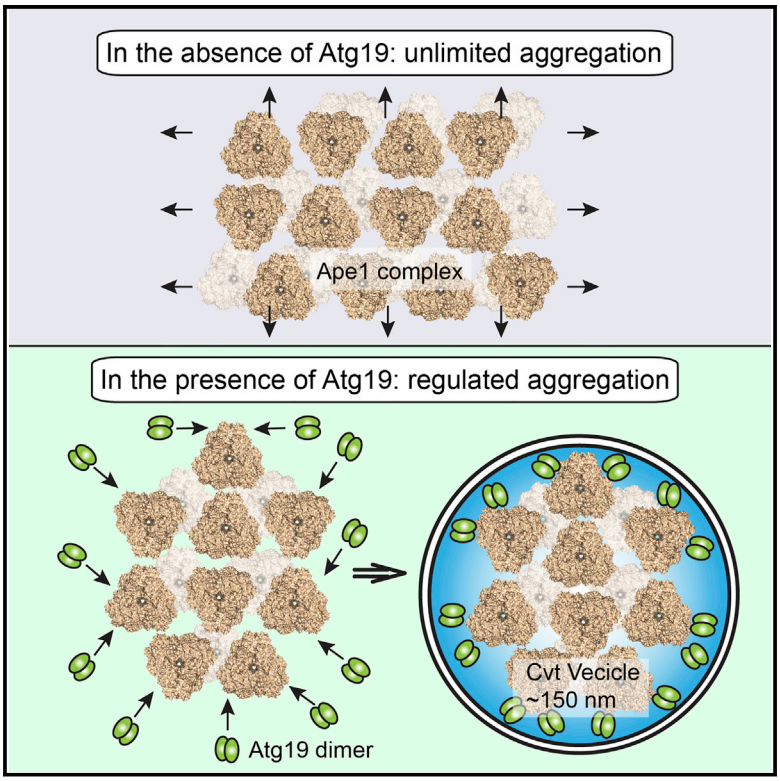

Authors

Akinori Yamasaki, Yasunori Watanabe, Wakana Adachi, ..., Yoshinori Ohsumi, Fuyuhiko Inagaki, Nobuo N. Noda

Correspondence

nn@bikaken.or.jp

In Brief

Yamasaki et al. report structural and functional studies to examine the mechanism underlying selective autophagy of Ape1, suggesting how Atg19 regulates the size of the Ape1 complex to be optimal for the Cvt pathway.

Highlights

- Crystal structure of prApe1 shows vertical projection of propeptides
- Self-assembled and Atg19-bound propeptides have a similar trimeric architecture
- Atg19 regulates the size of the Ape1 complex to be optimal for the Cvt pathway
- Atg19-blanketing of the Ape1 complex enables highly selective autophagy

Accession Numbers

5JH9
5JGF
5JHC
5JGE

Yamasaki et al., 2016, Cell Reports *16*, 19–27
June 28, 2016
http://dx.doi.org/10.1016/j.celrep.2016.05.066

Cell Reports
Report

Structural Basis for Receptor-Mediated Selective Autophagy of Aminopeptidase I Aggregates

Akinori Yamasaki,[1,6] Yasunori Watanabe,[1,6,7] Wakana Adachi,[2] Kuninori Suzuki,[3] Kazuaki Matoba,[1] Hiromi Kirisako,[4] Hiroyuki Kumeta,[2] Hitoshi Nakatogawa,[4] Yoshinori Ohsumi,[5] Fuyuhiko Inagaki,[1,2] and Nobuo N. Noda[1,*]
[1]Institute of Microbial Chemistry (BIKAKEN), Tokyo 141-0021, Japan
[2]Department of Structural Biology, Faculty of Advanced Life Science, Hokkaido University, Sapporo 001-0021, Japan
[3]Bioimaging Center, Graduate School of Frontier Sciences, University of Tokyo, Kashiwa 277-8562, Japan
[4]School of Life Science and Technology, Tokyo Institute of Technology, Yokohama 226-8503, Japan
[5]Unit for Cell Biology, Institute of Innovative Research, Tokyo Institute of Technology, Yokohama 226-8503, Japan
[6]Co-first author
[7]Present address: Faculty of Life Science, Kyoto Sangyo University, Kyoto 603-8555, Japan
*Correspondence: nn@bikaken.or.jp
http://dx.doi.org/10.1016/j.celrep.2016.05.066

SUMMARY

Selective autophagy mediates the degradation of various cargoes, including protein aggregates and organelles, thereby contributing to cellular homeostasis. Cargo receptors ensure selectivity by tethering specific cargo to lipidated Atg8 at the isolation membrane. However, little is known about the structural requirements underlying receptor-mediated cargo recognition. Here, we report structural, biochemical, and cell biological analysis of the major selective cargo protein in budding yeast, aminopeptidase I (Ape1), and its complex with the receptor Atg19. The Ape1 propeptide has a trimeric coiled-coil structure, which tethers dodecameric Ape1 bodies together to form large aggregates. Atg19 disassembles the propeptide trimer and forms a 2:1 heterotrimer, which not only blankets the Ape1 aggregates but also regulates their size. These receptor activities may promote elongation of the isolation membrane along the aggregate surface, enabling sequestration of the cargo with high specificity.

INTRODUCTION

Autophagy, an intracellular degradation system conserved across most eukaryotes, mediates various physiological processes and includes selective types of autophagy (Mizushima and Komatsu, 2011). An increasing number of substrates for selective autophagy, termed selective cargoes, have been identified and include various kinds of biomolecules, organelles, and even invasive bacteria (Randow and Youle, 2014; Suzuki, 2013). *Saccharomyces cerevisiae* aminopeptidase I (Ape1), a vacuolar enzyme, is one example of a factor that is thought to serve as selective cargo (Klionsky et al., 1992). Genetic, cell biological, and biochemical studies on the selective autophagy of Ape1 previously established the concept of receptor-mediated cargo selection during selective autophagy (Lynch-Day and Klionsky, 2010).

After translation in the cytoplasm, the precursor form of Ape1 (prApe1) spontaneously aggregates due to the presence of its propeptide (Kim et al., 1997). Ape1 aggregates are promptly and selectively transported to the vacuole through a specific type of selective autophagy, termed the cytoplasm-to-vacuole targeting (Cvt) pathway, during growth and through starvation-induced autophagy, where prApe1 is processed into a mature form (mApe1) lacking the propeptide by vacuolar hydrolases (Klionsky et al., 1992). The Cvt pathway and starvation-induced autophagy have important differences relative to each other. First, Cvt pathway-specific autophagosomes, termed Cvt vesicles, have a much smaller, uniform size (~150 nm) compared with starvation-induced autophagosomes (300–900 nm) (Baba et al., 1994; Noda et al., 2000). Second, Ape1 aggregates function as a scaffold for membrane biogenesis, and without them, Cvt vesicles are not formed (Shintani and Klionsky, 2004). Third, as Cvt vesicle membranes expand along the surface of Ape1 aggregates, most cytoplasmic components are excluded from the Cvt vesicle (Baba et al., 1997). The latter two features are also observed in selective autophagy of protein crystals (Tsutsui et al., 2015), peroxisomes, and invasive bacteria (the latter two were named pexophagy and xenophagy, respectively) (Manjithaya et al., 2010; Randow and Youle, 2014). In contrast, starvation-induced autophagosomes do not require cargoes as a scaffold for membrane biogenesis and engulf them together with other various cytoplasmic components.

Atg19 has been identified as a receptor for Ape1 (Leber et al., 2001; Scott et al., 2001). Atg19 contains a coiled-coil (CC), Atg11 binding region and Atg8-family interacting motif (AIM), and it tethers Ape1 to autophagic membranes through simultaneous interactions with Ape1 and lipidated Atg8 via the CC and AIM regions, respectively (Chang and Huang, 2007; Noda et al., 2010; Scott et al., 2001; Shintani et al.,2002; Yorimitsu and Klionsky, 2005). Although the structural basis of the Atg19^{AIM}-Atg8 interaction has been established (Noda et al., 2008), structural studies on the Atg19-Ape1 interaction are lacking.

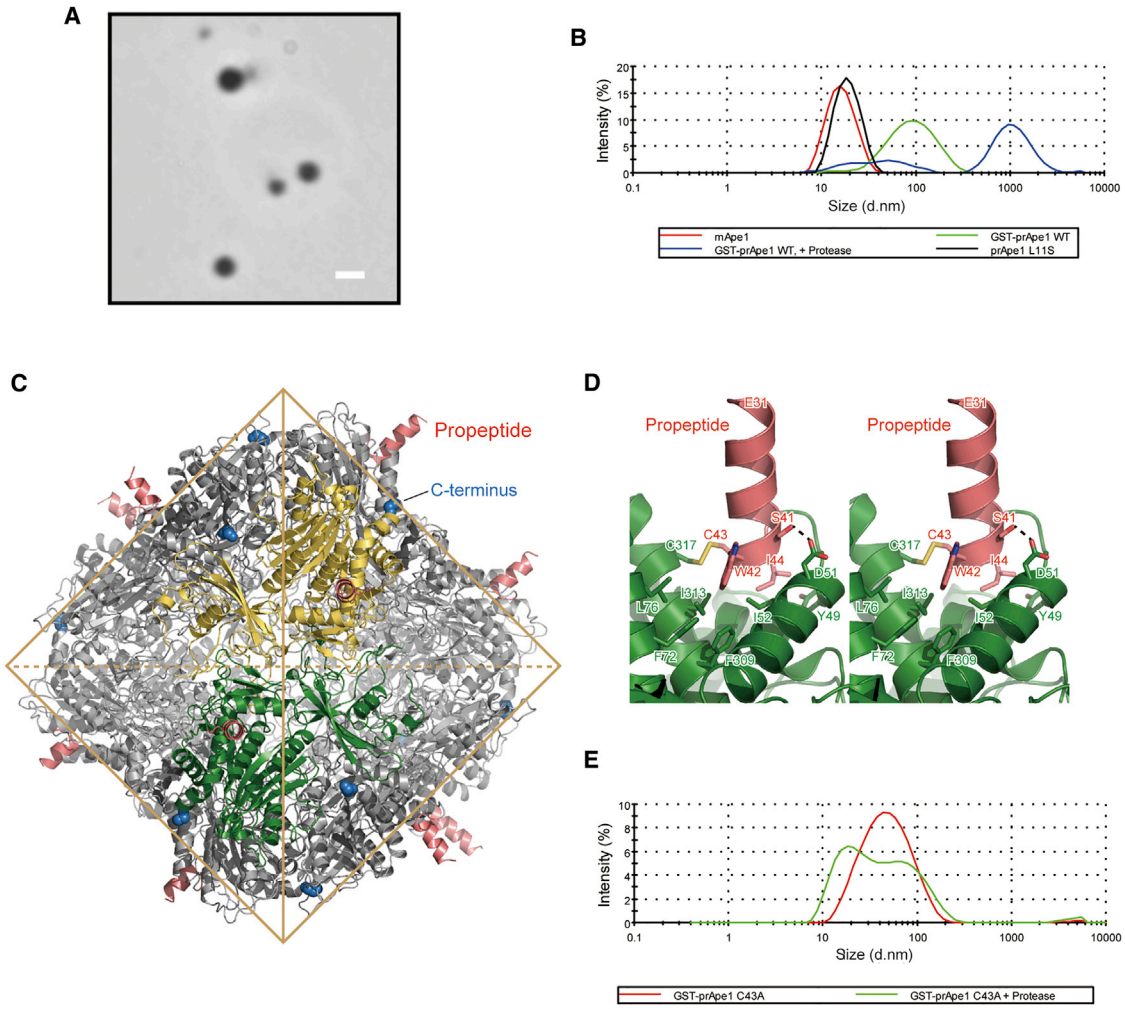

Figure 1. Crystal Structure of prApe1

(A) Microscopic observation of prApe1 aggregation in vitro that was caused by removing GST from prApe1. Scale bar, 1 μm.

(B) Size distribution of various Ape1 constructs measured by DLS. d.nm, apparent diameter (nm).

(C) Ribbon representation of the tetrahedral dodecameric architecture of prApe1 L11S. Yellow and dark green indicate two molecules with a 2-fold symmetry. Orange lines indicate the tetrahedron sides.

(D) Stereo view of the C-terminal portion of the propeptide.

(E) Size distribution of GST-prApe1 C43A with or without treatment with HRV 3C protease measured by DLS.

See also Figure S1.

Here, we report the crystal structures of full-length prApe1 and the propeptide in the self-assembled and Atg19-bound states. Structural data together with in vitro and in vivo experiments reveal features of both cargo and receptor, establishing the structural mechanisms underlying selective autophagy of Ape1.

RESULTS

Crystal Structure of prApe1

In order to establish the structural feature of the scaffolding selective cargo protein, we started a structural study on prApe1. Purified glutathione S-transferase (GST)-fused prApe1 was soluble, which immediately formed a large assemblage with a diameter of 1 μm upon cleavage of GST from prApe1 (Figures 1A and 1B, blue). GST-removed prApe1 was further assembled into a huge aggregate >100 μm by centrifugation (Figure S1A). In contrast, mApe1 showed good monodispersity, with a diameter of ~15 nm (Figure 1B, red). These observations suggest that the GST tag inhibited the aggregation of prApe1, and without the tag, prApe1 spontaneously forms an aggregate depending on the propeptide. The L11S mutation reportedly impairs the formation of the Ape1 complex in vivo (Oda et al., 1996; Shintani et al., 2002; Suzuki et al., 2002), and we confirmed that this mutation impaired the formation of prApe1 aggregates in vitro without a GST tag, whose size is similar to mApe1 (Figure 1B, black). Since wild-type (WT) prApe1 could not be subjected to crystallization trials due to aggregate formation, we crystallized and determined the structures of full-length

Ape1 (L11S) and WT mApe1 at a resolution of 2.1 and 1.83 Å, respectively (Table S1).

prApe1 formed a tetrahedral dodecamer in the crystal (Figure 1C), which was almost identical to that of mApe1 determined here and by another group, except for the propeptide portion (Figure S1B) (Su et al., 2015). The structure of the propeptide (residues 1–45) was previously predicted to have a helix-loop-helix conformation (Martinez et al., 1997; Oda et al., 1996). Among the 45 residues of the propeptide moiety, only the C-terminal portion (residues 31–45) had defined electron density and was modeled as an α helix, which corresponds to the second helix in the prediction (Figure 1C, red ribbons). The propeptide α helices were placed almost vertically relative to the tetrahedron enzyme body, although they are not involved in crystal packing (Figures 1C and S1C). A disulfide bond was formed between Cys43 of the propeptide and Cys317 of the enzyme body (Figure 1D). In addition, the side chains of Trp42 and Ile44 in the propeptide formed extensive interactions with the hydrophobic residues of the enzyme body. These interactions appeared to contribute to the vertical configuration of the propeptide. Dynamic light scattering (DLS) measurement showed that GST-prApe1 C43A was smaller than GST-prApe1 WT both before and after protease treatment (Figure 1E). Moreover, a C43A mutation partially impaired not only the dot formation of mCherry-prApe1 but also Ape1 maturation in vivo (Figures S1D–S1G), although the interaction with Atg19 was not affected (Figure S1H). These data suggest that the enzyme efficiently forms aggregates by presenting propeptides for self-assembly, which is important for the Cvt pathway to act efficiently.

Structural Basis of the Propeptide-Mediated Formation of the Ape1 Complex

The crystal structure of prApe1 L11S did not provide any information regarding the N-terminal region of the propeptide, which mediates the formation of the Ape1 complex (Oda et al., 1996; Seguí-Real et al., 1995) and Atg19 interaction (Shintani et al., 2002; Suzuki et al., 2002). In order to identify the residues in the propeptide that are directly involved in self-assembly and in Atg19 binding in solution, we performed nuclear magnetic resonance (NMR) studies on the N-terminal 45 residues of Ape1 ($Ape1^{N45}$). The narrow dispersion of the chemical shifts in the ^{1}H-^{15}N heteronuclear single quantum coherence (HSQC) spectrum of ^{15}N-labeled $Ape1^{N45}$ suggested that $Ape1^{N45}$ is largely unstructured at this concentration (25 μM) (Figure S2A). When the NMR spectrum was measured at a higher concentration (100 μM), some signals showed a reduction in intensity, which were clustered at the N-terminal region (residues 1–20) of the propeptide (Figure S2B). It was shown that the CC-containing region of Atg19 is responsible for prApe1 binding (Shintani et al., 2002). We narrowed the binding region for prApe1 and identified that the CC region (residues 160–187) of Atg19 ($Atg19^{CC}$) is sufficient for propeptide binding (see below). When non-labeled $Atg19^{CC}$ was titrated into ^{15}N-labeled $Ape1^{N45}$, the residues with weakened signals were again clustered at the N-terminal region (residues 1–20) of the propeptide (Figures S2C and S2D). These data clearly suggest that the N-terminal 20 residues of the propeptide are directly involved in both self-assembly and Atg19 binding.

Accordingly, we crystallized and determined the structure of $Ape1^{N22}$ alone and of the $Ape1^{N20}$-$Atg19^{CC}$ complex at 3.4 and 1.9 Å resolution, respectively (Table S1). For crystallization of $Ape1^{N22}$, the P22L mutant was used, because we found that this mutation induces an α-helical conformation of the propeptide and enhances self-assembly of propeptides in vitro (Figures S2E and S2F). The asymmetric unit of the $Ape1^{N22}$ crystal contained 39 peptide molecules, which could be grouped into 13 trimers (Figures S2G and S2H). Importantly, all of these trimers consisted of two parallel and one anti-parallel α helices. Previous ultracentrifugation studies showed that $Ape1^{N45}$ behaved as both a monomer (5.7–6.8 kDa) and a trimer (15.4–17.1 kDa) in the 45–210 μM concentration range (Su et al., 2015), supporting the idea that Ape1 propeptides form a homotrimer in solution as in Figure 2A.

The interactions underlying the $Ape1^{N22}$ P22L homotrimer were mostly hydrophobic and mainly mediated by Leu8, Leu11, Leu15, and Leu18 (Figure 2B). In contrast, there were few hydrophilic and no ionic interactions. These interactions buried a total surface area of 2,000–2,400 $Å^2$ of the three protomers. The highly hydrophobic nature of the trimer interface is consistent with the observation that high salt concentrations promote prApe1 aggregation (Morales Quinones et al., 2012; Scott et al., 2001). Moreover, the trimer structure can explain the severe defect and the enhancement of the Ape1 complex formation by L11S and P22L mutations (Figure S1D), as both residues are involved in the hydrophobic interactions constructing the trimer (Figure 2B). Thus, we concluded that the trimeric interactions of the propeptides are responsible for the formation of the Ape1 complex.

Structural Basis of prApe1 Recognition by Atg19

In the crystal of the $Ape1^{N20}$-$Atg19^{CC}$ complex, $Atg19^{CC}$ and $Ape1^{N20}$ formed two 2:1 heterotrimers that resemble one other (Figure S2I). We confirmed using analytical ultracentrifugation that the 2:1 mixture of $Atg19^{CC}$ and the propeptide behaved as a 14.1-kDa complex in solution, which is close to the theoretical value of a 2:1 complex (13.1 kDa) (Figure S2J). Both $Atg19^{CC}$ and $Ape1^{N20}$ had a single α-helical conformation, and intriguingly, they formed a heterotrimer consisting of two parallel α helices from $Atg19^{CC}$ and one anti-parallel α-helix from $Ape1^{N20}$ (Figure 2C), similar to the $Ape1^{N22}$ homotrimer (Figure 2A). Superimposition of the $Atg19^{CC}$-$Ape1^{N20}$ heterotrimer onto the $Ape1^{N22}$ homotrimer at the anti-parallel α helix showed that the two parallel α helices of $Atg19^{CC}$ and $Ape1^{N22}$ overlapped almost completely with each other (Figure S2K), strongly suggesting that the formation of the heterotrimer and homotrimer are mutually exclusive.

The interaction between $Atg19^{CC}$ and $Ape1^{N20}$ was mediated by many hydrophobic and hydrophilic interactions (Figure 2D). Among these, $Ape1^{N20}$ Arg5 played an especially important role, forming salt bridges and hydrogen bonds with Glu171, Asn175, and Glu178 of $Atg19^{CC}$. R5Q and L11S mutations in $Ape1^{N45}$ severely impaired the Atg19-$Ape1^{N45}$ interaction in vitro (Figure 2E), and Ala substitution at Glu171, Asn175, and Glu178 in Atg19 (3A mutation) abrogated the interaction between full-length prApe1 and Atg19 both in vitro and in vivo (Figures 2F and S2L). Moreover, we observed that Ape1 maturation was

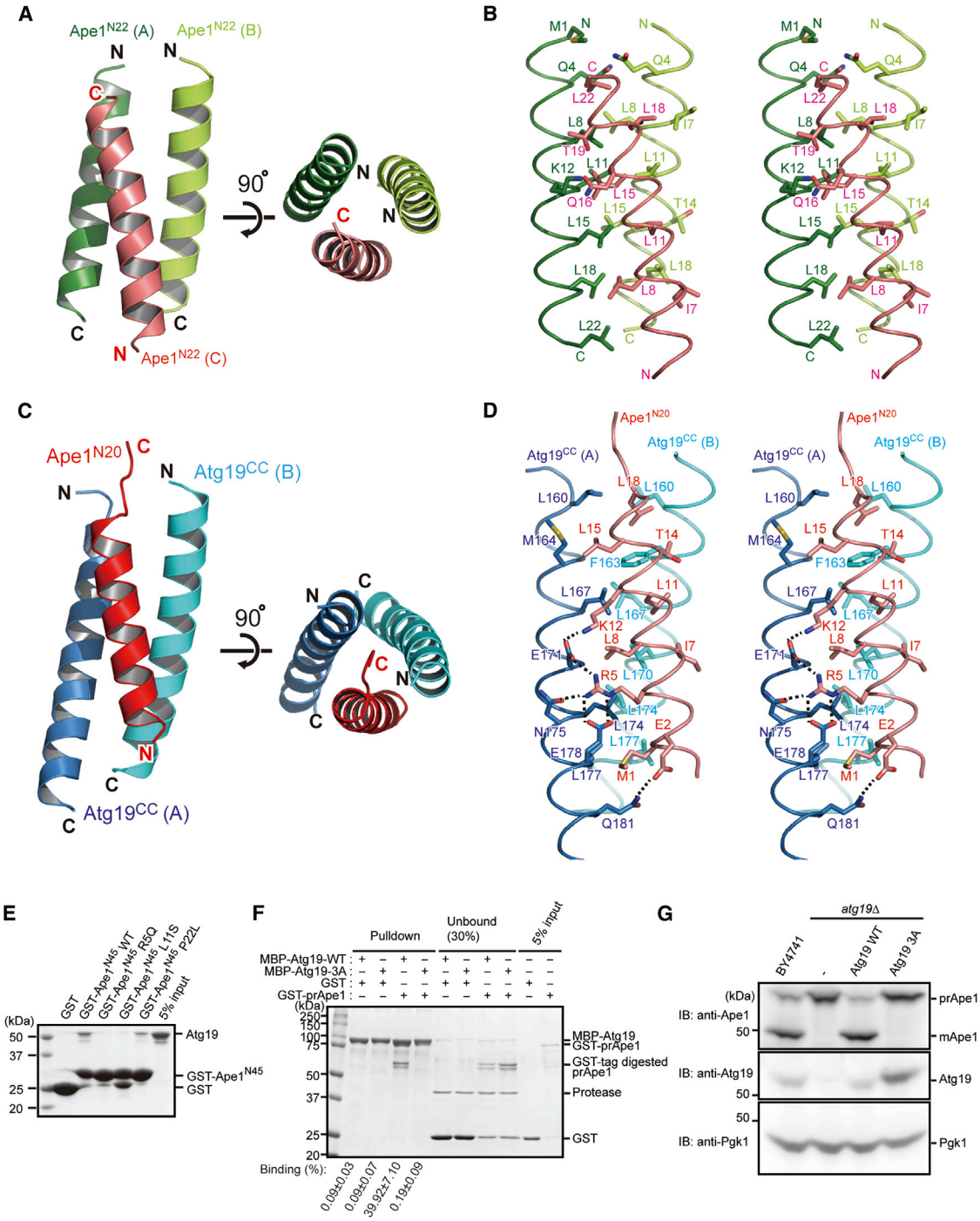

Figure 2. Structural Basis of Self-Assembly and Atg19 Binding of the Propeptide

(A) Crystal structure of a homotrimer of Ape1^{N22} P22L. N and C indicate the amino and carboxy termini, respectively.

(B) Stereo view of the interactions observed in the homotrimer of Ape1^{N22} P22L.

(C) Crystal structure of the Ape1^{N20}-Atg19^{CC} complex.

(D) Stereo view of the interactions observed in the Ape1^{N20}-Atg19^{CC} complex. The broken line represents possible hydrophilic interactions.

(E) In vitro pull-down assay between GST or GST-Ape1^{N45} variants and Atg19.

(F) In vitro pull-down assay between GST or GST-prApe1 and MBP-Atg19 variants. HRV 3C protease was added in order to separately detect prApe1 and MBP-Atg19 bands. The bound ratio of prApe1 is shown below the gel image.

(G) Yeast cell lysates from BY4741 derivative strains were immunoblotted with anti-Ape1 serum (top), anti-Atg19 antibody (middle), and anti-PGK1 antibody (bottom).

See also Figure S2.

completely impaired in *atg19*Δ cells expressing Atg19 3A (Figure 2G). These data reveal that in addition to the hydrophobic interactions, the salt bridges observed in the heterotrimer are essential for the Atg19-propeptide interaction and for Ape1 maturation. Formation of the heterotrimer buried a total surface area of 2,800–3,000 Å^2, which is larger than that buried in the Ape1^{N22} P22L homotrimer (2,400 Å^2 at the highest among 13 homotrimers). These data suggest that the interaction between Atg19^{CC} and Ape1^{N20} is stronger than propeptide self-assembly.

Atg19 Binding Inhibits the prApe1 Aggregation by Competing with Propeptide Self-Assembly

Structural data suggest that Atg19 would bind competitively to and inhibit the self-assembly of the propeptide. An in vitro pull-down assay and DLS showed that the interaction between GST-Ape1^{N45} and Ape1^{N45} was impaired by Atg19^{CC} (Figure 3A) and that the formation of a large assemblage of prApe1 upon cleavage of GST (Figures 1A and 1B) was impaired by Atg19^{CC} (Figure 3B). This inhibitory activity of Atg19^{CC} suggests that excess amounts of Atg19 would reduce the size of the Ape1 complex in vivo, thus impairing Ape1 maturation. We then followed the Ape1 complex using Ape1-mCherry in vivo, finding that the size of the Ape1 complex was affected by the amount of Atg19; it was increased in the absence of Atg19 and reduced under excess Atg19 (Figure 3C), though previous studies indicated that Atg19 overexpression did not affect Ape1 maturation in vivo (Baxter et al., 2005; Leber et al., 2001). We also performed similar experiments, which showed that overexpression of Atg19 WT, but not the 3A mutant that is unable to interact with prApe1, partially impaired Ape1 maturation in cells where endogenous Atg19 was expressed (Figures 3D and 3E). The discrepancy with the previous reports might be due to differences in the expression level of Atg19. This observation suggests that the excess binding of Atg19 to prApe1 inhibits the Cvt pathway by reducing the size of prApe1 aggregates.

Atg19 Blankets prApe1 Aggregates In Vivo

It is known that Atg19 binds to the surface of, but is not incorporated into, the Ape1 complex (Morales Quinones et al., 2012). In order to observe the localization of Atg19 in the Ape1 complex, we followed the distribution of Atg19-GFP in cells expressing excess amounts of prApe1 using the *CUP1* promoter, which leads to the formation of a giant Ape1 aggregate >1 μm in vivo (Suzuki et al., 2013). Atg19-GFP expressed from the endogenous promoter localized mainly to the surface of the giant Ape1 complexes, but not evenly (Figure 3F), possibly because the amount of Atg19 was insufficient for evenly blanketing these giant complexes. GFP-Atg19 was then overexpressed, and two types of prApe1 were also expressed: tag-free prApe1 was overexpressed in order to make a giant Ape1 complex, and RFP-Ape1 was expressed using the endogenous promoter in order to label the giant Ape1 complex. As expected, Atg19-GFP signals clearly and evenly blanketed the giant Ape1 complex (Figure 3G). In addition, GFP-Atg19 rings were sometimes observed inside the giant Ape1 complexes, and importantly, these rings did not contain RFP-Ape1 signals (Figures 3G and S3). We speculate that after blanketing most of the giant Ape1 complex, excess Atg19 deformed the surface of the complex, resulting in the formation of GFP-Atg19 rings. It should be noted that the size of the Ape1 complex containing Atg19 rings is significantly larger than that without Atg19 rings (Figure S3), suggesting that in cells expressing the endogenous level of Ape1, Atg19 localizes to the surface of the Ape1 complex. These data strongly suggested that Atg19 has the ability to blanket the Ape1 complex.

Atg19 Regulates the Size of the Ape1 Complex Optimal as a Selective Cargo

It is known that the diameter of Cvt vesicles is consistently 150 nm, which contrasts with the various sizes (300–900 nm) of starvation-induced autophagosomes (Baba et al., 1994; Noda et al., 2000). In order to reveal whether the size of prApe1 is important for the Cvt pathway, we tried to change the size of prApe1 aggregates without affecting Atg19 association. Since mutations that destroy propeptide self-assembly also impair Atg19 interaction, we designed a prApe1 mutant by fusing prApe1 to the Atg-protein-recruiting region (ARR; residues 363–415) of Atg19 that contains both Atg8 and Atg11 binding sites (prApe1-Atg19^{ARR}) (Figure 4A). In *atg19*Δ *ape1*Δ cells expressing prApe1-Atg19^{ARR}, efficient maturation of prApe1-Atg19^{ARR} was observed under rapamycin treatment conditions (Figure 4B, rapamycin 2 hr), suggesting that the Atg19^{ARR} moiety fused to prApe1 can, at least partially, complement the function of Atg19. However, this fusion protein was not delivered to the vacuole under growing conditions, suggesting that it could not behave as a scaffold for the Cvt pathway (Figure 4B, Growing). Since prApe1-Atg19^{ARR} lacks Atg19^{CC} that negatively regulates the size of prApe1 in vitro (Figure 3B), we speculated that the fusion protein became too large to be a target for the Cvt pathway. When Atg19^{CC}-GFP was co-expressed using the endogenous Atg19 promoter, maturation of prApe1-Atg19^{ARR} was observed even under growing conditions (Figure 4C, top). In these cells, free GFP was also observed (Figure 4C, top middle), implying that Atg19^{CC}-GFP bound to prApe1-Atg19^{ARR} was delivered to the vacuole through the Cvt pathway. The ability of prApe1-Atg19^{ARR} to bind Atg19^{CC} was confirmed by in vitro pull-down assay (Figure S4). Fluorescence microscopy also showed that prApe1-mCherry-Atg19^{ARR} was delivered to the vacuole when GFP-Atg19^{CC} was co-expressed but was rarely delivered without GFP-Atg19^{CC} co-expression (Figure 4D). A markedly bright dot of prApe1-mCherry-Atg19^{ARR} was frequently observed only in cells not expressing GFP-Atg19^{CC} (Figure 4D), suggesting that without Atg19^{CC}, prApe1-mCherry-Atg19^{ARR} cannot act as a cargo for the Cvt pathway, perhaps due to its size. Taken together, these data suggest that Atg19^{CC} binding to the propeptide of prApe1-Atg19^{ARR} regulates the size of this fusion protein, which enables it to function as a scaffold or a template for membrane biogenesis in the Cvt pathway.

DISCUSSION

Crystallographic studies showed that 12 copies of a propeptide protrude in a vertical manner from the tetrahedral dodecameric architecture of Ape1, and this involves a disulfide bond between the propeptide and enzyme body (Figures 1C and 1D), while isolated propeptides form a homotrimeric CC architecture with two parallel and one anti-parallel α helices (Figure 2A). These

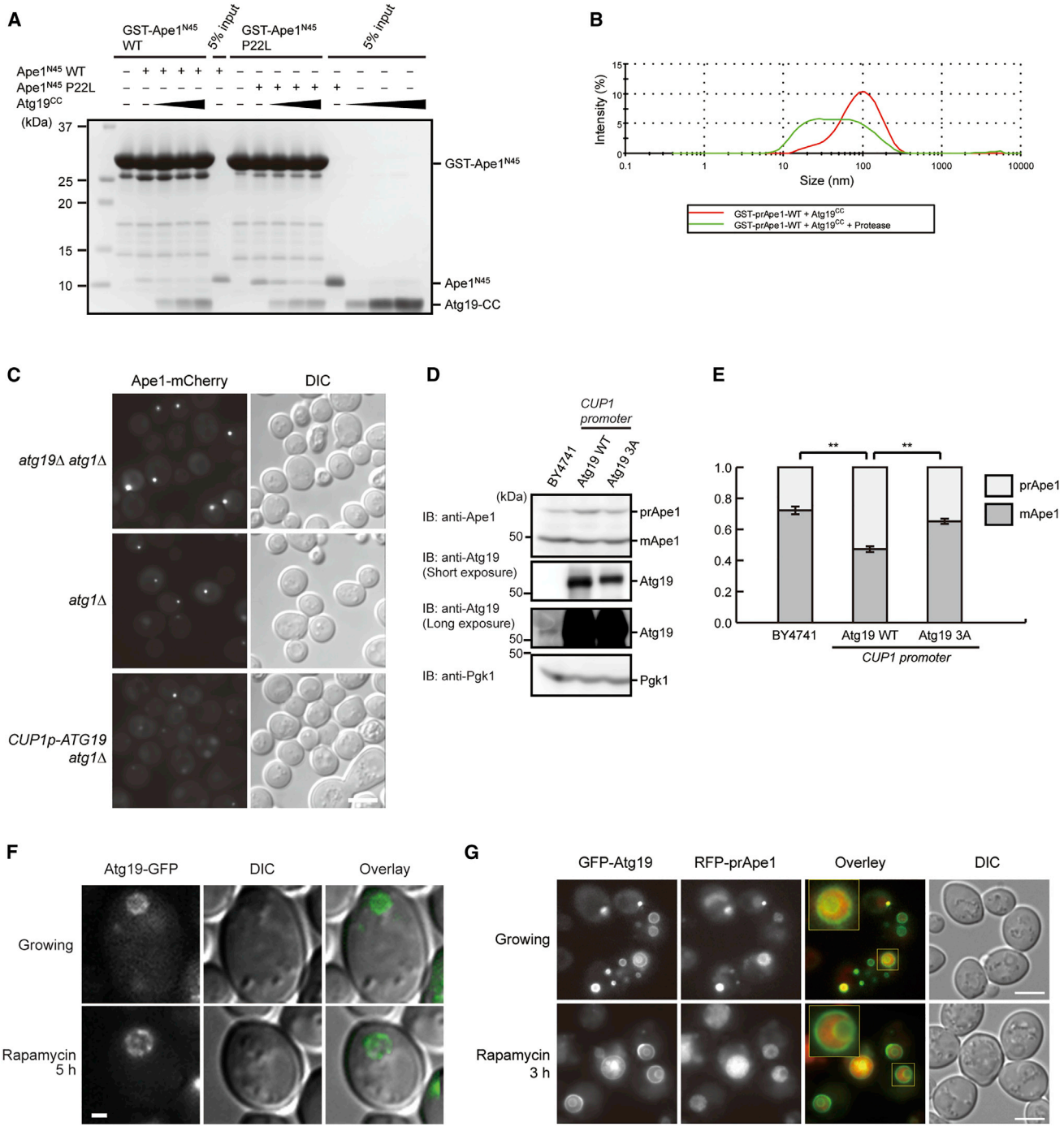

Figure 3. Atg19 Blankets the Ape1 Complex by Competing with Propeptide Self-Assembly

(A) In vitro pull-down assay between GST-Ape1^{N45} and Ape1^{N45} in the presence of 0, 10, 30, or 50 μg Atg19^{CC} (156–187).

(B) Size distribution of GST-prApe1 under the existence of Atg19^{CC} with or without protease treatment measured by DLS.

(C) Fluorescence microscopy to observe dot formation of Ape1-mCherry in *atg1*Δ *atg19*Δ (top) and *atg1*Δ (middle, bottom) cells expressing Atg19 under *CUP1* promoter (bottom). Scale bar, 5 μm.

(D) Lysates from BY4741 derivative strains expressing WT Atg19 and Atg19 3A under the *CUP1* promoter were immunoblotted with anti-Ape1 serum (top), anti-Atg19 antibody (top middle, short exposure; bottom middle, long exposure), and anti-PGK1 antibody (bottom).

(E) prApe1 and mApe1 bands in (D) were quantified and the average ratio of mApe1 and prApe1 obtained from three independent experiments are shown. **$p < 0.005$; error bars represent SD from three independent experiments.

(legend continued on next page)

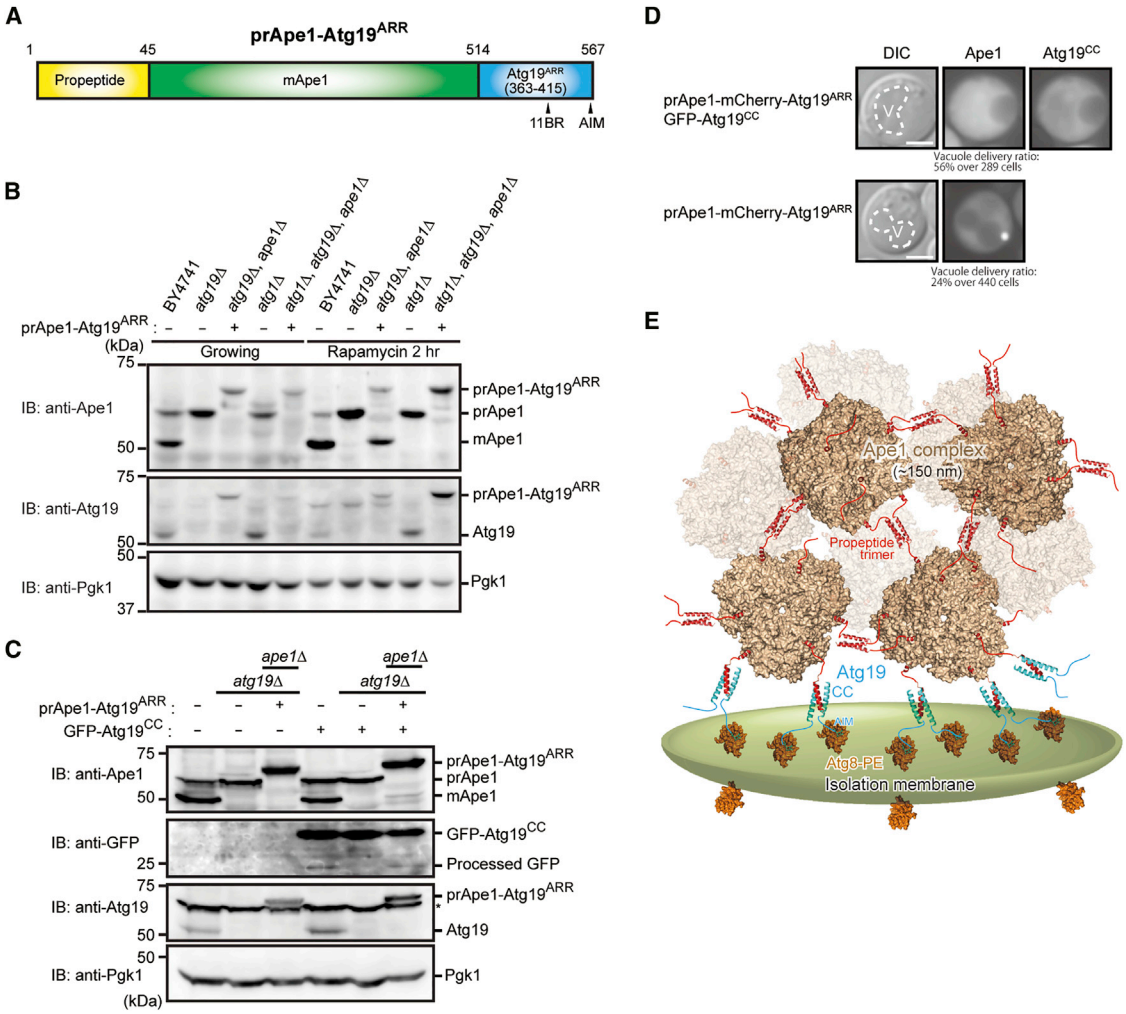

Figure 4. Atg19^{CC} Regulates the Size of prApe1 Aggregates Optimal for the Cvt Pathway

(A) Schematic diagram of prApe1-Atg19^{ARR} chimeric protein.

(B) BY4741 derivative strains with or without prApe1-Atg19^{ARR} expression were collected from a growing condition or after rapamycin treatment for 2 hr. The cell lysates were immunoblotted with anti-Ape1 serum (top), anti-Atg19 antibody (middle), and anti-PGK1 antibody (bottom).

(C) BY4741 derivative strains with or without prApe1-Atg19^{ARR} and/or GFP-Atg19^{CC} expression were collected from a growing condition. The lysates were immunoblotted with anti-Ape1 serum (top), anti-GFP antibody (top middle), anti-Atg19 antibody (bottom middle), and anti-PGK1 antibody (bottom).

(D) Observation of prApe1-mCherry-Atg19^{ARR} with or without co-expression of GFP-Atg19^{CC}. V indicates vacuole. Scale bars, 1 μm.

(E) Proposed model of the Ape1 complex and its sequestration by an isolation membrane during the Cvt pathway.

See also Figure S4.

structures suggest that prApe1 dodecamers are connected to one another through formation of a propeptide trimer, two from one dodecamer and one from another, which leads to the formation of prApe1 aggregates, named the Ape1 complex (Figure 4E).

The structure of the Atg19^{CC}-Ape1^{N20} complex showed striking similarity to the propeptide trimer, consisting of two parallel α helices from Atg19^{CC} and one anti-parallel α helix from Ape1^{N20} (Figure 2C), explaining the mutual exclusivity between propeptide self-assembly and Atg19 binding observed in vitro (Figure 3A). We argue that through binding competition, Atg19 negatively regulates prApe1 aggregation both in vitro and in vivo (Figures 3B and 3C). Importantly, the prApe1-Atg19^{ARR} fusion protein expressed in *atg19*Δ *ape1*Δ cells was delivered into the vacuole only when Atg19^{CC}-GFP was co-expressed (Figures

(F) Fluorescence microscopy to observe Atg19-GFP expressed at a natural level in cells overexpressing prApe1 before (top) and after treatment with rapamycin for 5 hr (bottom). Scale bar, 1 μm.

(G) Fluorescence microscopy to observe overexpressed GFP-Atg19 in cells overexpressing prApe1 and expressing RFP-Ape1 at a natural level before (top) and after treatment with rapamycin for 3 hr (bottom). Scale bar, 5 μm.

See also Figure S3.

4C and 4D). These observations establish an important role for Atg19 in the Cvt pathway other than specific recognition of prApe1, that is, regulating the size of prApe1 aggregates so they are optimal for transport into the vacuole.

Since Atg19-bound propeptides lose their ability to self-assemble, prApe1 aggregates cannot grow in the direction where Atg19 is bound. As a result, growth of prApe1 aggregates stops when they are surrounded by Atg19. On the basis of this mechanism, most Atg19 molecules eventually bind to the surface of the Ape1 complex, while little is incorporated inside it (Figure 3G). The ability of Atg19 to blanket the Ape1 complex and to bind Atg8-PE using AIM (Noda et al., 2008; Shintani et al., 2002) and additional binding sites at the ARR (Sawa-Makarska et al., 2014) would enable the isolation membrane to expand along the surface of the Ape1 complex while excluding most cytoplasmic components under growing conditions (Figure 4E). Thus, Atg19 possesses the sophisticated ability to function as a receptor for selective autophagy that excludes most of the cytoplasmic components other than the specific cargo.

EXPERIMENTAL PROCEDURES

X-Ray Crystallography

All recombinant proteins were expressed using *Escherichia coli* BL21. Purification was performed by affinity chromatography and size exclusion chromatography. Crystallization was performed by the sitting-drop vapor diffusion method at 20°C. Diffraction data were collected at beamlines NE3A and NW12A at KEK, Japan, or at beamline BL41XU at SPring-8, Japan. Structure determination was performed by single anomalous dispersion method for the $Ape1^{N20}$-$Atg19^{CC}$ complex, by single isomorphous replacement with anomalous scattering for $Ape1^{N22}$ P22L, and by the molecular replacement method for mApe1 and prApe1 L11S. Further detailed procedures are described in Supplemental Experimental Procedures.

Functional Analyses

NMR spectra were obtained at 25°C on Varian Unity Inova 600 spectrometers. DLS was measured at 25°C using Zetasizer nano S (Malvern). CD spectra were measured at 20°C using a J-720W spectropolarimeter (Jasco). Analytical ultracentrifugation was performed at 20°C using Optima XL-I (Beckman Coulter). Pull-down assays were performed using glutathione Sepharose 4B (GE Healthcare), GST-accept (Nakacali Tesque), or Amylose resins (New England Biolabs). Yeast experiments were performed using the stains listed in Table S2. Further detailed procedures are described in Supplemental Experimental Procedures.

ACCESSION NUMBERS

The accession numbers for the crystal structures of prApe1, mApe1, $Ape1^{N22}$, and $Ape1^{N20}$-$Atg19^{CC}$ reported in this paper are PDB: 5JH9, 5JGF, 5JHC, and 5JGE, respectively.

SUPPLEMENTAL INFORMATION

Supplemental Information includes Supplemental Experimental Procedures, four figures, and two tables and can be found with this article online at http://dx.doi.org/10.1016/j.celrep.2016.05.066.

AUTHOR CONTRIBUTIONS

A.Y., Y.W., W.A., K.M., and N.N.N. performed crystallographic studies. Y.W., H. Kumeta, and F.I. performed NMR studies. A.Y., K.S., and N.N.N. performed in vitro experiments. A.Y., K.S., H. Kirisako, and H.N. performed yeast experiments. A.Y., Y.W., K.S., H.N., Y.O., F.I., and N.N.N. analyzed data. A.Y. and N.N.N. wrote the manuscript, all authors discussed the results and commented on the manuscript, and N.N.N. supervised the work.

ACKNOWLEDGMENTS

We thank Dr. F. Arisaka (Nihon University) for analytical ultracentrifugation experiments. Synchrotron radiation experiments were performed at beamline BL41XU at SPring-8, Japan and NE3A, NW12A, at KEK, Japan. This work was supported by CREST, JST (N.N.N., F.I., and H.N.), a research grant from the Astellas Foundation for Research on Metabolic Disorders (to N.N.N.), a research grant from the Takeda Science Foundation (to K.S.), Japan Society for the Promotion of Sciences (JSPS) KAKENHI grants-in-aid for Scientific Research (B) (25291040 to K.S.), for Young Scientist (A) (25711005 to H.N.), for Young Scientist (B) (15K21608 to K.M.), for Specially Promoted Research (23000015 to Y.O.), and for Scientific Research on Priority Areas (25111003 to H.N., 25111004 to N.N.N., and 26111505 to K.S.), the Targeted Proteins Research Program (Y.O. and F.I.), and Platform for Drug Discovery, Informatics, and Structural Life Science (to N.N.N.) from the Ministry of Education, Culture, Sports, Science, and Technology of Japan.

Received: January 25, 2016
Revised: April 29, 2016
Accepted: May 16, 2016
Published: June 16, 2016

REFERENCES

Baba, M., Takeshige, K., Baba, N., and Ohsumi, Y. (1994). Ultrastructural analysis of the autophagic process in yeast: detection of autophagosomes and their characterization. J. Cell Biol. *124*, 903–913.

Baba, M., Osumi, M., Scott, S.V., Klionsky, D.J., and Ohsumi, Y. (1997). Two distinct pathways for targeting proteins from the cytoplasm to the vacuole/lysosome. J. Cell Biol. *139*, 1687–1695.

Baxter, B.K., Abeliovich, H., Zhang, X., Stirling, A.G., Burlingame, A.L., and Goldfarb, D.S. (2005). Atg19p ubiquitination and the cytoplasm to vacuole trafficking pathway in yeast. J. Biol. Chem. *280*, 39067–39076.

Chang, C.Y., and Huang, W.P. (2007). Atg19 mediates a dual interaction cargo sorting mechanism in selective autophagy. Mol. Biol. Cell *18*, 919–929.

Kim, J., Scott, S.V., Oda, M.N., and Klionsky, D.J. (1997). Transport of a large oligomeric protein by the cytoplasm to vacuole protein targeting pathway. J. Cell Biol. *137*, 609–618.

Klionsky, D.J., Cueva, R., and Yaver, D.S. (1992). Aminopeptidase I of Saccharomyces cerevisiae is localized to the vacuole independent of the secretory pathway. J. Cell Biol. *119*, 287–299.

Leber, R., Silles, E., Sandoval, I.V., and Mazón, M.J. (2001). Yol082p, a novel CVT protein involved in the selective targeting of aminopeptidase I to the yeast vacuole. J. Biol. Chem. *276*, 29210–29217.

Lynch-Day, M.A., and Klionsky, D.J. (2010). The Cvt pathway as a model for selective autophagy. FEBS Lett. *584*, 1359–1366.

Manjithaya, R., Nazarko, T.Y., Farré, J.C., and Subramani, S. (2010). Molecular mechanism and physiological role of pexophagy. FEBS Lett. *584*, 1367–1373.

Martinez, E., Jimenez, M.A., Seguí-Real, B., Vandekerckhove, J., and Sandoval, I.V. (1997). Folding of the presequence of yeast pAPI into an amphipathic helix determines transport of the protein from the cytosol to the vacuole. J. Mol. Biol. *267*, 1124–1138.

Mizushima, N., and Komatsu, M. (2011). Autophagy: renovation of cells and tissues. Cell *147*, 728–741.

Morales Quinones, M., Winston, J.T., and Stromhaug, P.E. (2012). Propeptide of aminopeptidase 1 protein mediates aggregation and vesicle formation in cytoplasm-to-vacuole targeting pathway. J. Biol. Chem. *287*, 10121–10133.

Noda, T., Kim, J., Huang, W.P., Baba, M., Tokunaga, C., Ohsumi, Y., and Klionsky, D.J. (2000). Apg9p/Cvt7p is an integral membrane protein required for

transport vesicle formation in the Cvt and autophagy pathways. J. Cell Biol. *148*, 465–480.

Noda, N.N., Kumeta, H., Nakatogawa, H., Satoo, K., Adachi, W., Ishii, J., Fujioka, Y., Ohsumi, Y., and Inagaki, F. (2008). Structural basis of target recognition by Atg8/LC3 during selective autophagy. Genes Cells *13*, 1211–1218.

Noda, N.N., Ohsumi, Y., and Inagaki, F. (2010). Atg8-family interacting motif crucial for selective autophagy. FEBS Lett. *584*, 1379–1385.

Oda, M.N., Scott, S.V., Hefner-Gravink, A., Caffarelli, A.D., and Klionsky, D.J. (1996). Identification of a cytoplasm to vacuole targeting determinant in aminopeptidase I. J. Cell Biol. *132*, 999–1010.

Randow, F., and Youle, R.J. (2014). Self and nonself: how autophagy targets mitochondria and bacteria. Cell Host Microbe *15*, 403–411.

Sawa-Makarska, J., Abert, C., Romanov, J., Zens, B., Ibiricu, I., and Martens, S. (2014). Cargo binding to Atg19 unmasks additional Atg8 binding sites to mediate membrane-cargo apposition during selective autophagy. Nat. Cell Biol. *16*, 425–433.

Scott, S.V., Guan, J., Hutchins, M.U., Kim, J., and Klionsky, D.J. (2001). Cvt19 is a receptor for the cytoplasm-to-vacuole targeting pathway. Mol. Cell *7*, 1131–1141.

Seguí-Real, B., Martinez, M., and Sandoval, I.V. (1995). Yeast aminopeptidase I is post-translationally sorted from the cytosol to the vacuole by a mechanism mediated by its bipartite N-terminal extension. EMBO J. *14*, 5476–5484.

Shintani, T., and Klionsky, D.J. (2004). Cargo proteins facilitate the formation of transport vesicles in the cytoplasm to vacuole targeting pathway. J. Biol. Chem. *279*, 29889–29894.

Shintani, T., Huang, W.P., Stromhaug, P.E., and Klionsky, D.J. (2002). Mechanism of cargo selection in the cytoplasm to vacuole targeting pathway. Dev. Cell *3*, 825–837.

Su, M.Y., Peng, W.H., Ho, M.R., Su, S.C., Chang, Y.C., Chen, G.C., and Chang, C.I. (2015). Structure of yeast Ape1 and its role in autophagic vesicle formation. Autophagy *11*, 1580–1593.

Suzuki, K. (2013). Selective autophagy in budding yeast. Cell Death Differ. *20*, 43–48.

Suzuki, K., Kamada, Y., and Ohsumi, Y. (2002). Studies of cargo delivery to the vacuole mediated by autophagosomes in Saccharomyces cerevisiae. Dev. Cell *3*, 815–824.

Suzuki, K., Akioka, M., Kondo-Kakuta, C., Yamamoto, H., and Ohsumi, Y. (2013). Fine mapping of autophagy-related proteins during autophagosome formation in Saccharomyces cerevisiae. J. Cell Sci. *126*, 2534–2544.

Tsutsui, H., Jinno, Y., Shoda, K., Tomita, A., Matsuda, M., Yamashita, E., Katayama, H., Nakagawa, A., and Miyawaki, A. (2015). A diffraction-quality protein crystal processed as an autophagic cargo. Mol. Cell *58*, 186–193.

Yorimitsu, T., and Klionsky, D.J. (2005). Atg11 links cargo to the vesicle-forming machinery in the cytoplasm to vacuole targeting pathway. Mol. Biol. Cell *16*, 1593–1605.